Journal of Materials Chemistry C

ROYAL SOCIETY OF CHEMISTRY

PAPER

View Article Online
View Journal | View Issue

Cite this: J. Mater. Chem. C, 2025, 13, 22788

ortho-Halogen functionalized *N*-squaraines: structure–property relationship and dual-mode colorimetric and fluorometric sulfide ion detection

Premie P. Fernandes,[a] Ankitha M. Shenoy,[a] Vratta Grover,[b] Naveena S. Veeranagaiah[c] and Vellanki Lakshmi *[a]

Symmetric *ortho*-halogen derivatives of anilinium *N*-squaraines were synthesized and characterized using ^{1}H-NMR, mass, FT-IR, and single-crystal X-ray diffraction techniques. The effect of halogen substituents (–F, –Cl, –Br, –I) on the optoelectronic and electrochemical properties of *N*-squaraines has been thoroughly investigated. Additionally, the theoretical calculations demonstrated that the *ortho* functionalization slightly lowers the HOMO–LUMO energy band gap, which aligns with the optical band gap. Moreover, the solid-state photophysical characterization revealed that the photo-excited state remains a singlet, even in the presence of heavy atoms like bromine and iodine. The solid-state fluorescence emission was also significantly higher than in the solution state, with the quantum yields soaring up to 24%. Further, the two acidic binding sites in the synthesized compounds **2–5** were evaluated for anion sensing. The *o*-halo-derivatives act as selective dual-mode colorimetric and "Turn-On" fluorometric chemosensors for sulfide anions, with the solution changing from colorless to yellow and a four-fold enhanced emission intensity. Furthermore, adding acid makes the solution turn colorless again, as investigated in detail using the *o*-chloro-derivative. The chemosensor displayed good reversibility for up to seven cycles and demonstrated applications in molecular logic gates.

Received 4th July 2025,
Accepted 15th October 2025

DOI: 10.1039/d5tc02572a

rsc.li/materials-c

Introduction

Squaraines (SQs) constitute 1,3-disubstituted squaric acid derivatives containing two electron-donating substituents adjoining an electron-deficient squaryl ($C_4O_2^-$) centre.[1] SQ dyes are a distinctive class of polymethine dyes with a resonance-stabilized zwitterionic structure wherein electrons are highly delocalized over the conjugated bridge.[2] Ever since the late 1990s, SQs have been employed in optoelectronic applications, prominently photovoltaics, solar cells, and semiconductors.[2–5] But, in the last decade, biomedical and material science applications of SQs have been an emerging trend.[2,6] Currently, SQs are widely a part of active fluorescent ion-transporters and bioimaging.[7,8] The SQ dyes are formed by the condensation of squaric acid and electron-rich arenes, whereas a condensation between squaric acid and aniline derivatives yields Schiff bases called 1,3-bis-(phenylamino)-squaraines, due to the nucleophilic attack *via* the lone pair of nitrogen on the carbonyl carbon of squaric acid, also termed as *N*-Squaraines.[9] *N*-Squaraines are donor–acceptor–donor conjugated (D–π–A–π–D) compounds which, upon deprotonation, transform into an A–π–A–π–A type system.[1] *N*-squaraines are a fascinating class of dyes with relatively broad absorption and moderate molar extinction coefficients ($\approx 3 \times 10^4$ M^{-1} cm^{-1}).[9] While *N*-squaraines have been less explored, they have been developed as sensors for selective analyte detection. Due to their strong optical properties, these highly responsive probes have been employed to detect metal ions, anions, and CO_2 gas.[9,10]

Sulfide presents a fascinating dichotomy in biological systems and environmental contexts. Within living tissues, it is endogenously produced by cystathionine enzymes and plays an important role in regulating normal physiological processes, including cell growth, vasodilation, neuromodulation of the brain, anti-oxidation, anti-inflammation, *etc.*[11,12] Moreover, sulfide has demonstrated significant therapeutic potential in the treatment of skin-related disorders.[13] However, sulfide also represents a serious environmental hazard, often found in sewage and wastewater effluents. It is generated in large quantities through various industrial processes, including coal tar production, sewage treatment, petroleum products, natural

[a] Synthesis and Materials Laboratory, Department of Chemistry, National Institute of Technology Karnataka, Surathkal–575025, India. E-mail: lakshmi.vellanki@nitk.edu.in
[b] Department of Chemistry, Indian Institute of Technology Bombay, Powai, Mumbai, 400076, India
[c] Department of Chemistry, Central University of Karnataka, Kalaburagi, Karnataka, 585367, India

gas processing, and biogas production.[14] Chronic exposure to sulfide may disrupt metabolic pathways in living organisms and can lead to adverse biological complications such as liver cirrhosis, suffocation, hypertension, hyperglycemia, atherosclerosis, Down syndrome, Alzheimer's disease, and Huntington's disease.[15–18] At exposure to less than 100 ppm levels, discomfort including eye and throat irritation, headache, nausea, chest tightness, *etc.*, has been reported, whereas exposure above 1000 ppm levels may result in respiratory depression followed by unconsciousness, and can be fatal.[19,20] Consequently, monitoring sulfide ion concentrations becomes extremely crucial for the safety of industrial workers.

In the past few decades, numerous analytical methods, such as electrochemical sensors, gas chromatography, colorimetry, inductively coupled plasma-atomic emission spectroscopy, voltammetry, and semiconductor metal oxide-based sensors, have been utilized for the detection of sulfide.[21–25] However, colorimetric and fluorescence-based probes have gained immense popularity owing to their ease of operation, quick response time, low cost, high sensitivity, and non-destructive nature.[26–28] Fluorescence probes have been employed for *in vitro* and *in vivo* bioimaging, thereby increasing their applicability.[28,29] Presently, various small molecules, such as benzoxadiazoles, coumarin, BODIPY, 1,8-naphthalimides, Schiff bases, azo dyes, rosamine, fluorescein, organo-copper complexes, and organo-lanthanide complexes, have shown sensing potential towards sulfide.[30–40] Conversely, *N*-squaraine dyes haven't been exploited for their potential in detecting sulfide ions, especially in biological systems, and though a number of fluorometric sulfide sensors have been developed, their selectivity over biothiols and other anions, along with response time, is a serious limitation. Therefore, the development of superior probes is still necessary for use in biological, industrial, and environmental setups.[41]

In view of developing fluorescent probes for sulfide sensing applications and taking into account the existing literature on *N*-squaraines, we synthesized and characterized *N*-squaraines comprising a central squaryl core and two aniline aryl rings with *ortho*-substituted electron-withdrawing halogens (F, Cl, Br, I) (Chart 1). Notably, the synthesized compounds showcased significant solid-state emissive behavior. Further, these compounds have been investigated thoroughly for their potential sensing properties towards anions, wherein highly sensitive dual-mode colorimetric and fluorometric detection of sulfide anions was observed. It is interesting to note that this work is the first example of *N*-squaraine derivatives to be exploited as a dual-mode colorimetric and fluorometric sensor for sulfide anions. Finally, their applications in molecular logic gates have been elucidated in this work.

Experimental section

Materials and methods

The materials and methods for the experiments are given in the SI.

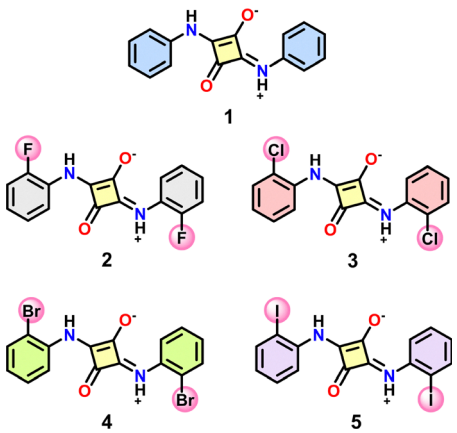

Chart 1 Anilinium *N*-squaraine and its *o*-halogen substituted derivatives.

Synthesis and characterization

General procedure. Squaric acid (1 equiv., 0.44 mmol) and the corresponding *o*-haloaniline (4 equiv., 1.75 mmol) were taken in a mixture of *n*-butanol and toluene (1 : 1, 8 mL) in a 25 mL round-bottom flask and refluxed under a nitrogen atmosphere for 12 h. The reaction mixture was cooled, and the solid obtained was filtered using a Buchner funnel followed by sequential washings with hot ethyl acetate (10 mL), chloroform (15 mL), petroleum ether (10 mL), and *n*-pentane (2 mL). The obtained precipitate was dried in a vacuum oven at 90 °C to obtain the final pure product.

Compound ***1.*** (*E*)-3-Oxo-2-(phenylamino)-4-(phenylimino) cyclobut-1-en-1-olate was synthesized as per the reported literature.[42] The title compound was obtained as a pale-yellow solid with 86% yield. ^{1}H NMR (400 MHz, DMSO-d_6) δ (ppm): 11.43 (br s, 2H), 7.86–7.65 (m, 4H), 7.38 (t, J = 7.8 Hz, 4H), 7.13 (t, J = 7.3 Hz, 2H). HRMS (ESI) m/z: $[M + H]^+$ calculated for $C_{16}H_{12}N_2O_2$ 265.0980, found 265.0979. FT-IR (ATR, cm^{-1}): 3241 (N–H); 3176, 3127, 3087, 3057, 2993, 2964, 2929 (=C–H); 1617 (C=N); 1586 (C=O); 1545 (N–H, bending); 1498, 1449, 1421, 1408 (C–C); 1337, 1245 (C–N); 822, 794, 763, 747, 684 (C–H, bending). λ_{abs} (DMSO) = 388 nm. λ_{em} (DMSO) = 416, 436 nm.

Compound ***2.*** (*E*)-2-((2-Fluorophenyl)amino)-4-((2-fluoro phenyl)iminio)-3-oxocyclobut-1-en-1-olate was obtained as a shiny light orange crystalline solid in 80% yield. ^{1}H NMR (400 MHz, DMSO-d_6) δ (ppm): 11.41 (br s, 2H), 7.66 (t, J = 8.0 Hz, 2H), 7.35–7.15 (m, 6H). HRMS (ESI) m/z: $[M + H]^+$ calculated for $C_{16}H_{10}N_2O_2F_2$ 301.0780, found 301.0779. FT-IR (ATR, cm^{-1}): 3240 (N–H); 3197, 3142, 3073, 2990, 2969 (=C–H); 1615 (C=N); 1596 (C=O); 1537 (N–H, bending); 1493, 1457, 1371 (C–C); 1299, 1256 (C–N); 1088 (C–F); 829, 782, 730 (C–H, bending). λ_{abs}(DMSO) = 373 nm. λ_{em}(DMSO) = 417 nm, 434 nm.

Compound ***3.*** (*E*)-2-((2-Chlorophenyl)amino)-4-((2-chloro phenyl)iminio)-3-oxocyclobut-1-en-1-olate was obtained as a shiny orange crystalline solid with 71% yield. ^{1}H NMR (400 MHz, DMSO-d_6) δ (ppm): 11.22 (br s, 2H), 7.54 (ddd, J = 11.9, 8.0, 1.5 Hz, 4H), 7.37 (td, J = 7.7, 1.5 Hz, 2H), 7.28 (td, J = 7.7, 1.6 Hz, 2H).

HRMS (ESI) *m*/*z*: $[M + H]^+$ calculated for $C_{16}H_{10}N_2O_2Cl_2$ 333.0189, found 333.0189. FT-IR (ATR, cm^{-1}): 3218 (N–H); 3176, 3111, 3064, 2963 (═C–H); 1596 (C═N); 1580 (C═O); 1522 (N–H, bending); 1475, 1417 (C–C); 1293, 1234 (C–N); 815 (C–Cl); 766, 753, 683 (C–H, bending). λ_{abs}(DMSO) = 369 nm. λ_{em}(DMSO) = 414 nm, 433 nm.

Compound ***4***. (*E*)-2-((2-Bromophenyl)amino)-4-((2-bromo phenyl)-iminio)-3-oxocyclobut-1-en-1-olate was obtained as a shiny dark orange crystalline solid with 76% yield. ^{1}H NMR (500 MHz, DMSO-d_6) δ (ppm): 11.11 (br s, 2H), 7.68 (dd, J = 8.0, 1.4 Hz, 2H), 7.52 (dd, J = 8.0, 1.6 Hz, 2H), 7.41 (td, J = 7.7, 1.4 Hz, 2H), 7.21 (td, J = 7.7, 1.6 Hz, 2H). HRMS (ESI) *m*/*z*: $[M + H]^+$ calculated for $C_{16}H_{10}N_2O_2Br_2$ 422.9155, found 422.9154. FT-IR (ATR, cm^{-1}): 3214 (N–H); 3176, 3108, 3058, 2959 (═C–H); 1595 (C═N); 1577 (C═O); 1511 (N–H, bending); 1470, 1413 (C–C); 1285, 1234 (C–N); 813, 798, 752 (C–H, bending); 652 (C–Br). λ_{abs}(DMSO) = 369 nm. λ_{em}(DMSO) = 414, 431 nm.

Compound ***5***. (*E*)-2-((2-Iodophenyl)amino)-4-((2-iodophenyl) iminio)-3-oxocyclobut-1-en-1-olate was obtained as a yellowish-green solid with a 65% yield. ^{1}H NMR (400 MHz, DMSO-d_6) δ (ppm): 10.98 (br s, 2H), 7.88 (d, J = 7.8 Hz, 2H), 7.46–7.37 (m, 4H), 7.03 (ddd, J = 8.5, 6.7, 2.3 Hz, 2H). MALDI-TOF MS *m*/*z*: $[M + Na]^+$ calculated 539.07, found 539.077. FT-IR (ATR, cm^{-1}): 3205 (N–H); 3174, 3113, 2965 (═C–H); 1595 (C═N); 1574 (C═O); 1514 (N–H, bending); 1464, 1417 (C–C); 1284, 1232 (C–N); 814, 766, 755 (C–H, bending); 520 (C–I). λ_{abs}(DMSO) = 375 nm. λ_{em}(DMSO) = 422, 435 nm.

Sensing studies. Sodium salts of different anions like acetate, arsenite, arsenate, fluoride, chloride, bromide, iodide, hypochlorite, carbonate, dihydrogen phosphate, bicarbonate, bisulfate, azide, nitrite, nitrate, phosphate, sulfide, thiosulfate, and sulfate were prepared in deionized water. For probe **3**, a stock solution of 10^{-5} M in DMSO was prepared and used for sensing studies.

Results and discussion

Symmetrical *N*-squaraines (**1–5**) synthesized by the condensation of the squaric acid with corresponding *o*-halo substituted aniline at 120 °C for 12 h in a 1 : 1 mixture of *n*-butanol and toluene solvents yielded 65–86% (Scheme 1). These compounds exhibited solubility in polar aprotic solvents like *N*,*N*-dimethylformamide (DMF) and dimethyl sulfoxide (DMSO) only upon heating, indicating their high polarity. Further, compounds **1–5** were characterized by ^{1}H-NMR, mass, and FT-IR spectroscopic techniques (Fig. S1–S10). The ^{1}H-NMR spectrum of compound **1** showed three sets of signals for ten phenyl protons and one signal for the two –NH protons.

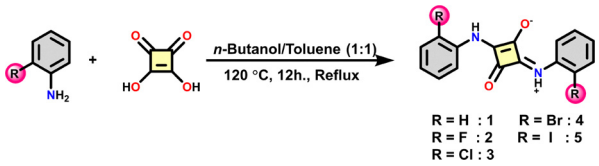

Scheme 1 Synthesis of *N*-squaraine derivatives, **1–5**.

The overlay of ^{1}H-NMR spectra of compounds **1–5** showed that incorporating halo-substitution at the *ortho* position led to significant changes in their spectral splitting pattern (Fig. 1). Compounds **2–5** exhibited three to five sets of signals in the range of 7.0–12.0 ppm corresponding to eight phenyl protons and one set for the two –NH protons due to the symmetrical nature of the compounds **2–5**. An upfield shift in the –NH peak was observed from **2** to **5** with decreasing electronegativity of the halo-derivatives. The –NH protons of compounds **2** and **3** showed a slight upfield shift of 0.02 ppm and 0.21 ppm, respectively, compared to compound **1**. Compounds **4** and **5** bearing bromo and iodo substituents exhibited broader –NH peaks with a more upfield shift of 0.32 ppm and 0.45 ppm, respectively. FT-IR spectroscopy provided supplementary structural characteristic insights for the synthesized compounds (Fig. S11). The halo-substituted derivatives exhibited their characteristic peaks of C–F at 1088 cm^{-1} in compound **2**, C–Cl at 815 cm^{-1} in compound **3**, C–Br at 652 cm^{-1} in compound **4**, and C–I at 520 cm^{-1} in compound **5**, significantly impacted the vibrational frequencies of C═N in the region of 1595–1617 cm^{-1} and C═O in the region of 1574–1596 cm^{-1}. Notably, a shift in the stretching vibrational frequencies from 3241 cm^{-1} to 3205 cm^{-1} and bending vibrational frequencies from 1545 cm^{-1} to 1514 cm^{-1} for the N–H linkages in compounds **1–5** was observed.

Single-crystal X-ray structure

The solid-state structure of compound **2** was determined using single-crystal X-ray diffraction analysis. Yellow-colored rectangular crystals suitable for diffraction studies were obtained through slow crystallization from a dimethyl sulfoxide and methanol (1 : 2) solution over fifteen days. The single-crystal X-ray diffraction data revealed that compound **2** crystallizes in the monoclinic space group, $P2_1/n$ (Fig. S12 and Tables S1–S4). Fig. 2A presents both top and side views of the ORTEP diagram at a 50% probability level of the crystal structure, along with the unit cell packing diagram (Fig. 2B), which exhibits a herringbone-like arrangement with face-to-face π–π stacking interactions (Fig. 2C). The molecules adopt a dimeric arrangement, where the arene rings are slightly twisted out of plane relative to the squaryl moiety, with a torsional angle of −14.12° (C7–N1–C1–C2) (Table S4). The π–π interactions within these dimers have an interplanar distance of 3.514 Å (Table S5), indicating a slightly offset stacking rather than perfect face-to-face overlap. In addition to π-stacking, the structure is further stabilized by two C═O···H–N intermolecular hydrogen bonds (2.093 Å) (Table S6) and two weak edge-to-face interactions that contribute to the observed herringbone-like packing motif, which is known to aid in preventing fluorescence quenching by minimizing aggregation-induced non-radiative decay. The fluorine atoms at the *ortho* positions also interact with the phenyl hydrogen (2.661 Å) and NH group hydrogen (2.421 Å), further enhancing the crystal stability.

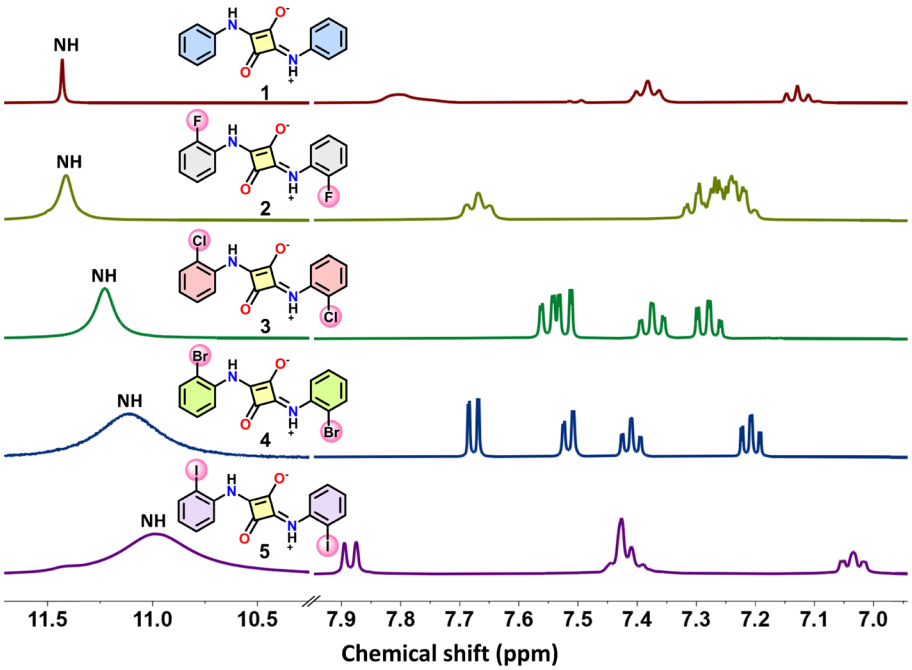

Fig. 1 Overlay of normalized ^{1}H-NMR spectra of compounds **1–5** in DMSO-d_6.

Hirshfeld surface (HS) analysis provided a better understanding of the intermolecular interactions within the crystal (Fig. S13). HS of compound **2** was mapped over d_{norm}, curvedness, and shape index, which features a transparent surface to aid in the visualization of key moieties involved in hydrogen bonding interactions.[43] Intermolecular hydrogen bonding interactions such as C–O···H, N–H···O were evident by intense red spots observed on the d_{norm} HS, and the percentage of each interaction is mapped as sharp spikes in the 2D fingerprint plots (Fig. S13 and S14). The shape index mapping showed distinct complementary red and blue triangular regions elucidating face-to-face π–π stacking interactions. The curvedness property confirmed the presence of π–π stacking interactions, as indicated by the flat green regions observed over the aromatic ring contacts in the crystal structure. The 2D fingerprint plots revealed that the O···H interaction contributed 13.3% to the HS, whereas C···H, F···H, N···H, and C···O contributed 17.4%, 13.8%, 2.4% and 1.7% respectively, to the HS (Fig. S14).

Photophysical and electrochemical properties

UV-visible absorption properties of compounds **1–5** were studied in DMSO solvent and presented in Fig. 3 and Table 1. The unsubstituted compound **1** exhibited absorbance maxima (λ_{max}) at 388 nm. Compounds **2–5** exhibited a major absorption band between 369–375 nm attributed to π–π* transition and a minor peak at higher energy, 268–278 nm. The introduction of halo substitution at the *ortho* position of aniline showed a hypsochromic shift of about 13–19 nm in its absorption spectra compared to that of the parent compound **1**. A pronounced hypsochromic shift of 19 nm was observed for compounds **3** and **4** with Cl and Br, respectively. Steady-state fluorescence data were obtained in DMSO solvent for compounds **1–5** upon excitation (λ_{exc}) at λ_{max}. Compounds **2–5** exhibited emission peaks ($\lambda_{exc} = \lambda_{max}$) in the range of 414–422 nm, which showed a blue shift of ∼14–22 nm compared to parent compound **1** (436 nm) in DMSO solvent. The maximum blue shift of 22 nm was observed for compounds **3** and **4** compared to compound **1**. All the compounds **2–5** in the solution state exhibited fluorescence with splitting emission bands (Fig. 3), which can be attributed to intramolecular charge transfer (ICT) transitions from the donor phenyl moieties to the acceptor squaryl unit. Compound **1–5** exhibited poor fluorescence quantum yield, Φ_f less than 1% (Table 1).

The electrochemical properties of compounds **1–5** were evaluated by cyclic voltammetry in anhydrous DMF solution using tetrabutylammonium perchlorate (TBAP) as a supporting electrolyte at room temperature with a scan rate of 200 mV s^{-1} (Fig. 4). Herein, we examined the effect of *o*-halogen substitution in compounds **2–5** through the change in the redox properties compared to the parent compound **1**. The electron-withdrawing nature of halogen substituents significantly influences the electron density around the imine (C═N) linkage with respect to compound **1**. Compound **1** exhibited one irreversible oxidation onset at 0.51 V and one reversible reduction potential at −1.02 V. Relatively, the halogen-functionalized compounds **2–5** demonstrated negligible differences in their reduction and oxidation potentials. Compounds **2–5** displayed one quasi-reversible oxidation potential in the range of 0.45–0.49 V, indicating easier oxidation compared to **1** (Fig. 4 and Table 1). Similarly, compounds **2–5** showed reversible reduction potentials at −1.03 V, −1.05 V, −1.02 V, and −1.04 V, respectively. This implies that halogenated compounds **2–5** were slightly more difficult to reduce compared to compound **1**. Thus, the electrochemical studies indicated that the redox

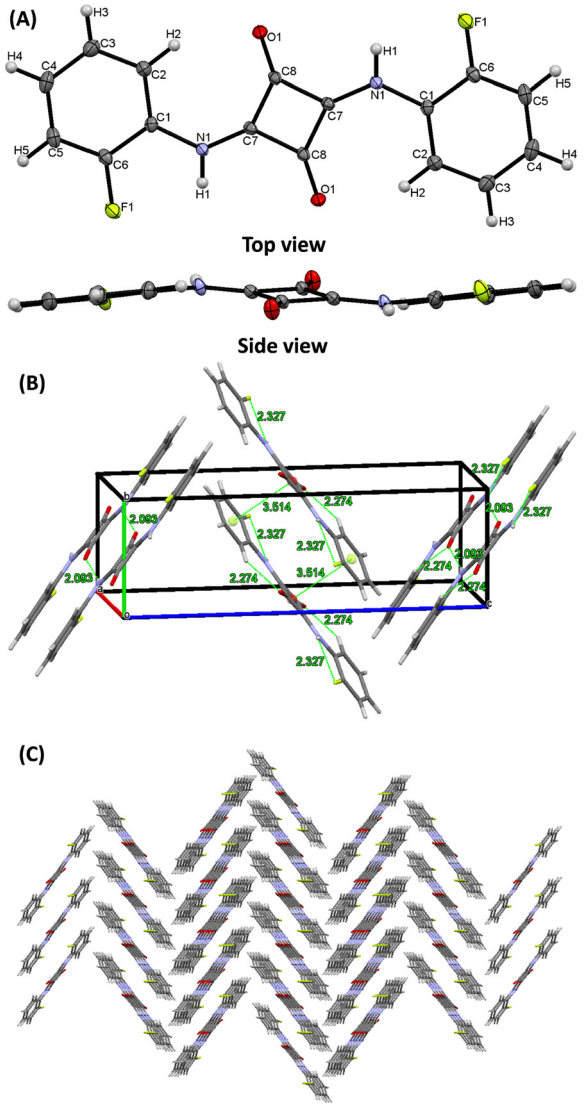

Fig. 2 (A) Top (up) and side (down) view of ORTEP diagram of compound **2** with 50% probability level, (B) packing diagram in a unit cell, and (C) herringbone-type arrangement viewed along *a*-axis.

potentials of compound **1** were altered considerably due to different halogens at the *ortho* position.

Theoretical calculations

To gain a deeper insight into the photophysical properties and the band gap energy between the highest occupied molecular orbital (HOMO) and the lowest unoccupied molecular orbital (LUMO), density functional theory (DFT) calculations were performed using the Gaussian 09 package with B3LYP functional and DGDZVP basis set. The geometries of compounds **1–5** were optimized using B3LYP-DGDZVP, and then the absorption properties were computed using TDA energy calculations with DMSO solvent. Table S7 presents the principal orbital transitions, calculated absorption maxima values, and oscillator strength (*f*) values. The calculated and observed λ_{max} values on comparison were found to be relatable. The molecular

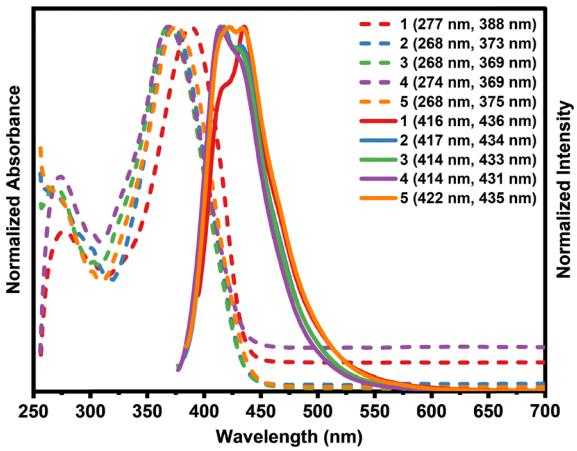

Fig. 3 Normalized absorption (dashed line) and emission (solid line) spectra of compounds **1–5** (10^{-5} M) in DMSO solution.

orbital energy diagram of optimized geometries for compounds **1–5** showed a slight change in the HOMO–LUMO band gap energy of 3.42 eV for compound **1** to 3.39–3.36 eV in compounds **2–5** (Fig. 5). The TD-DFT studies confirm the presence of strong intramolecular charge transfer (ICT) transitions present in the *N*-squaraines, which was validated by spatially distinct HOMOs and LUMOs indicating charge distribution, strong $S_0 \rightarrow S_1$ transition, and high oscillator strengths. The charge separation in the electron density mapped with electrostatic potential (ESP) surface plot indicates that the *ortho* halogen insertion in anilinium *N*-squaraines further enhances intramolecular charge transfer (ICT) present in the squaryl moiety (Fig. S15).[44] Compounds **1–5** distinctly display an electron-dense region over the oxygen atoms on the squaryl moiety. In compound **1**, the dark blue portion, which is the electron-donating region, is spread over the –NH group and the neighboring –CH of the phenyl ring. Compounds **2–5** displayed gradually fading positive electrostatic potentials over the –NH regions, becoming nearly neutral in compound **5**, indicating that *o*-halogenation aids in suppressing the electrophilic properties of the parent compound **1**. This also implies that the basicity of the –NH proton decreases gradually from compounds **1–5**, which is an added advantage for selective anion sensing.

Solid-state photophysical studies

The solid-state photophysical studies of compounds **1–5** were examined to identify their emissive behavior. Compound **1** exhibited two broad absorption peaks at 309 nm and 368 nm, while compounds **2–5** showed peaks in the range of 419–439 nm (Fig. S16). Interestingly, when exposed to UV radiation of 365 nm, compounds **1–5** showed intense solid-state fluorescence, with **1** emitting green, **2** as bright yellow, **3** as yellow, **4** as yellow, and **5** as green (Fig. 6). The steady-state fluorescence emission spectra were obtained for the compounds by exciting at λ_{max} of absorbance to get further insights into their electronic properties. Compounds **1–5** exhibited broad emission peaks in the range of 469–488 nm (Fig. 7). Compound **1** showed an

Table 1 Photophysical and electrochemical properties of compounds **1–5**

No.	R	λ_{max}[a] (nm)/ε ($\times 10^4$ M^{-1} cm^{-1})	λ_{em}[ab] (nm)	$\Delta\upsilon_{st}$[c] (cm^{-1})	Φ_f[d] (%)	ΔE_g[e] (eV)	E_{ox}[f] (V)	E_{red}[g] (V)	λ_{max}[h] (nm)/ε ($\times 10^4$ M^{-1} cm^{-1})	λ_{em}[h] (nm)	$\Delta\upsilon_{st}$[c] (cm^{-1})	Φ_f[i] (%)	ΔE_g[j] (eV)
1	H	388 (2.76)	416, 436	1735	0.2	3.20	0.51	−1.02	461 (2.21)	513	2200	3	2.69
2	F	373 (2.31)	417, 434	2855	0.6	3.32	0.45	−1.03	466 (4.41)	520	2228	6	2.66
3	Cl	369 (2.92)	414, 433	2945	0.5	3.36	0.47	−1.05	464 (4.12)	529	2646	4	2.67
4	Br	369 (2.47)	414, 431	2945	0.4	3.36	0.49	−1.02	469 (4.45)	509	1672	3	2.64
5	I	375 (2.95)	422, 435	2969	0.2	3.31	0.47	−1.04	472 (1.37)	496	1025	2	2.63

[a] Measured in DMSO solution (10^{-5} M). [b] $\lambda_{exc} = \lambda_{max}$. [c] Stokes shift. [d] Absolute fluorescence quantum yield in DMSO solvent. [e] HOMO–LUMO bandgap energy calculated by the absorption maxima peak in DMSO according to $E_g = hc/\lambda_{max} = 1240/\lambda_{max}$. [f] E_{ox} = the irreversible onset and reversible half-wave oxidation potentials (V *vs.* Ag/Ag^+). [g] E_{red} = the reversible half-wave reduction potentials (V *vs.* Ag/Ag^+), performed in 0.06 M TBAP in anhydrous DMF, scan rate 200 mV s^{-1}. [h] Measured in 99 : 1 v/v 10^{-5} M DMSO–H_2O (0.1 M NaOH) solution. [i] Absolute fluorescence quantum yield in 99 : 1 v/v 10^{-5} M DMSO–H_2O (0.1 M NaOH) solution. [j] HOMO–LUMO bandgap energy calculated by the absorption maxima peak in 99 : 1 DMSO–H_2O (0.1 M NaOH) according to $E_g = hc/\lambda_{max} = 1240/\lambda_{max}$.

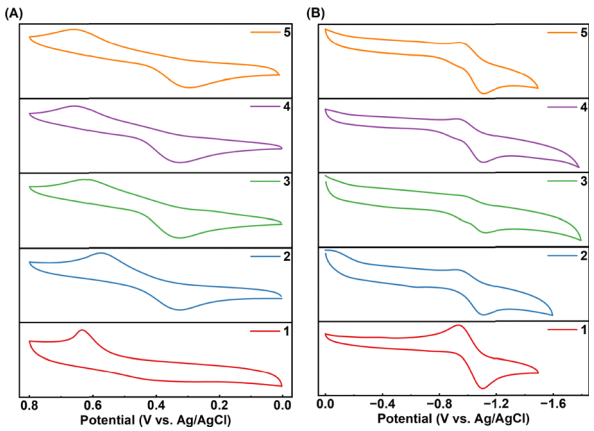

Fig. 4 Overlay of (A) oxidation and (B) reduction cyclic voltammograms of compounds **1–5** in anhydrous DMF using 0.06 M tetrabutylammonium perchlorate as a supporting electrolyte at 200 mV s^{-1} scan rate.

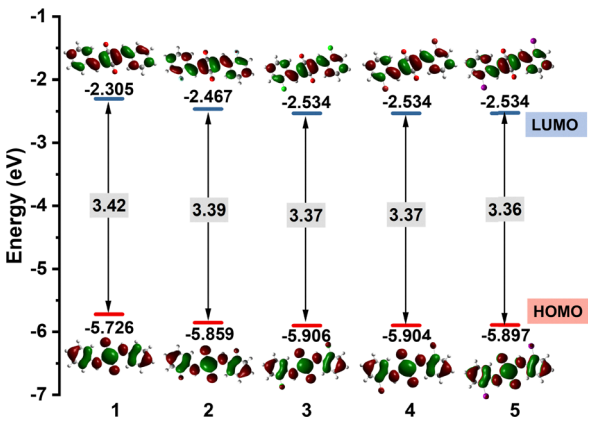

Fig. 5 Molecular orbital (MO) energy diagram with HOMOs and LUMOs of optimized geometries of compounds **1–5**.

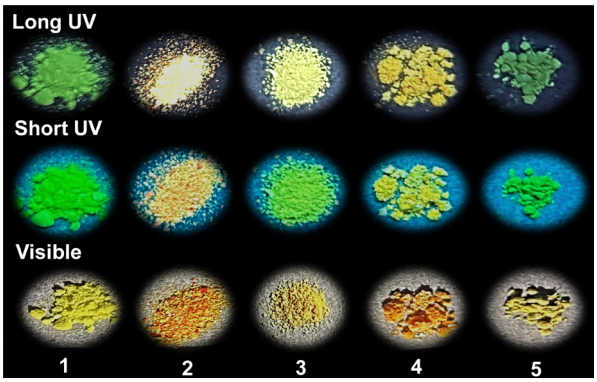

Fig. 6 Images of compounds **1–5** from left to right under long UV lamp (365 nm), short UV lamp (254 nm), and naked eye.

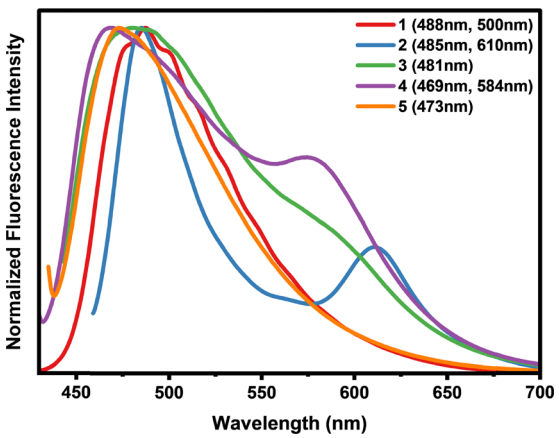

Fig. 7 Normalized intensity spectra of compounds **1–5** in solid state ($\lambda_{exc} = \lambda_{max}$).

emission band at 488 nm with a quantum yield (Φ_f) of 3%, whereas compounds **2–5** exhibited emission bands in the range of 468–610 nm. Incorporating an electronegative substituent at the *ortho* position significantly improved solid-state emission. Compound **2** exhibits a ten-fold increase in quantum yield in comparison to compound **1**, with Φ_f value of 24%. Compound **2** exhibited the highest fluorescence intensity due to the halogen effect driven by the highly electronegative fluorine atom. Compounds **3** and **4** both exhibited Φ_f of 7% and compound **5** exhibited the least fluorescence intensity with Φ_f of 2% due to the heavy atom effect of the iodine substituent.[45]

The lifetimes of compounds **1–5** were studied in the solid state by exciting at λ_{max} of absorbance using the Time-correlated single photon counting (TCSPC) technique to get

further insights into electronic properties. The fitted decay curves are represented in Fig. S17, which reveals that the photo-excited state in **1–5** remains singlet in the solid state, even with the presence of heavy atoms like bromine and iodine, which aligns with the quantum yields. All the compounds showed bi-exponential decay, and the average lifetimes of the fitted data are represented in Table S9. All the halogen-derived compounds **2–5** exhibited increased fluorescence lifetime, τ_1 in the range of 0.34–1.00 ns in comparison to compound **1**, which showed 0.43 ns. Compound **2** showed the highest τ_1 of 1.00 ns, with the highest quantum yield of 24%.

UV-vis and fluorescence upon the action of NaOH

Upon the addition of a strong base, 0.1 M NaOH in 10^{-5} M DMSO solution of compounds **1–5** in the ratio 99 : 1 v/v of DMSO : NaOH, showed a prominent color change from colorless to yellow visible to the naked eye. The UV-visible spectroscopic studies revealed a single absorbance band at 461–472 nm with a significant bathochromic shift of ~90 nm compared to solutions without NaOH (Fig. S18). The complete disappearance of peaks in the 366–383 nm region for all compounds **1–5** upon the addition of base indicates that there is complete deprotonation of the iminium ion (=NH^+) and imine linkage (–NH–), leading to dianion formation, as shown in Scheme S1.[1,46] The bathochromic shift in the absorption band in compounds **1–5** upon the addition of NaOH is due to the extended π-conjugation in the system caused by the deprotonation.[46] Fluorescence emission studies for these NaOH-added solutions showed that the fluorescence intensity is enhanced significantly (Fig. S19), which can be attributed to strong intramolecular charge transfer (ICT) as a result of deprotonation within the system. Compounds **2** and **3** emit intense green and bright yellow fluorescence, respectively, at longer wavelengths than the other compounds, **1**, **4**, and **5** (Fig. S19). From the fluorescence spectra, a 10^{-5} M DMSO solution of compound **2** containing 1% 0.1 M NaOH showed the highest fluorescence intensity with an emission peak at 520 nm with respect to other compounds **1**, **3–5** (Fig. S18B and S19). In comparison to compound **1**, compound **2** showed nearly 2.5-fold increased emission intensity, whereas compound **3**, with 1% 0.1 M NaOH, showed almost two-fold enhanced emission intensity at 529 nm. Moreover, the intensity of the wavelength maxima of compounds **4** and **5** decreased drastically upon adding NaOH. Further, a spectroscopic study carried out by varying the percentages of NaOH from 1% to 99% v/v in a 10^{-5} M DMSO solution of compound **3** revealed that the fluorescence intensity was maximum at 1% NaOH concentration (Fig. S20). Fluorescence quantum yields, Φ_f for compounds **1–5** in 99 : 1 v/v DMSO : NaOH solutions were determined by the absolute method. Compound **1** showed Φ_f of 3%, and in the presence of halogens at the *ortho* position, compounds **2** and **3** showed the highest Φ_f of 6% and 4%, respectively (Table 1). Compared to compounds **1–3**, **4** and **5** showed a decrease in the Φ_f, which may be attributed to the heavy-atom effect of bromine and iodine. Additionally, DFT calculations on compounds **1–5** in their deprotonated form were studied with respect to their neutral form in DMSO solvent (Fig. S21). The HOMO–LUMO band gaps narrowed down significantly in the deprotonated form to ~2.9 eV from ~3.4 eV in the neutral form. Narrowing of band gaps was accompanied by increased π-conjugation as demonstrated by more delocalized molecular orbitals across the conjugated backbone, giving rise to the red-shifted absorption and emission properties.

Anion-sensing studies

The colorimetric and fluorometric detection ability of chemosensor compounds **2–5** was examined in 10^{-5} M DMSO solution towards various anions such as acetate, arsenite, arsenate, fluoride, chloride, bromide, iodide, hypochlorite, carbonate, dihydrogen phosphate, bicarbonate, bisulfate, azide, nitrite, nitrate, phosphate, sulfide, thiosulfate, and sulfate. 100 equivalents of various anion solutions were added to a 3 mL solution of compounds **2–5** (10^{-5} M, DMSO) (Fig. S22–S24). Compounds **2–5** exhibited selective detection towards sulfide anions and the sensing mechanism was studied in detail for compound **3** based on the quantum yield, Φ_f enhancement for compounds **2** and **3** as described for the interaction with hydroxide ion (Fig. S19 and Table 1). The free compound **3** in 10^{-5} M DMSO is colorless, and upon the addition of sulfide, the color changed to yellow with yellow fluorescence (Fig. 8). The addition of other anions did not exhibit any color change, except methoxide and hydroxide, thus confirming the inactivity of the chemosensor **3** to detect other anions (Fig. S25). Further, UV-visible absorption and fluorescence spectroscopy were used to validate the preliminary conclusions made by visualizing the color changes (Fig. S22 and S24). The sulfide anions caused changes in the spectral pattern of compound **3** solutions, and the observed bathochromic shift further confirmed the sensitivity of chemosensor compound **3** towards detecting this anion. Furthermore, the minimum response time for the colorimetric detection of sulfide anions was less than 5 seconds, confirming the rapid sensing of sulfide anions by changing the color of the chemosensor solution. The selectivity of probe **3** for sulfide ion (S^{2-}) detection can be attributed to the high basicity of S^{2-}. The basicity hierarchy of common anions is as follows: $S^{2-} > PO_4^{3-} > AsO_4^{3-} > CO_3^{2-} > ClO^- > HCO_3^- > CH_3COO^- > N_3^- > NO_2^- > F^- > H_2PO_4^- > HSO_4^- > SO_4^{2-} > S_2O_3^{2-} > NO_3^- > Cl^- > Br^- > I^-$. The pronounced difference in the basicity of anions enables the compound **3** to distinguish selectively sulfide ion among the other potentially interfering anions.

To analyze the binding properties of chemosensor compound **3** towards selective sensing of sulfide anions, the sensor was titrated systematically with sulfide, and the changes were monitored using UV-visible spectra (Fig. 8A). A two-step change of the absorption bands is seen upon careful analysis of the UV-visible absorption spectra. Firstly, the absorbance at 369 nm decreased gradually up to the addition of 64 equiv. of sulfide and a new peak at 464 nm started to appear with clear isobestic points at 333 nm and 423 nm, as seen in the inset of Fig. 8A. Secondly, upon further addition of sulfide anions step-wise, the absorption intensity at 369 nm continued to decrease, and a

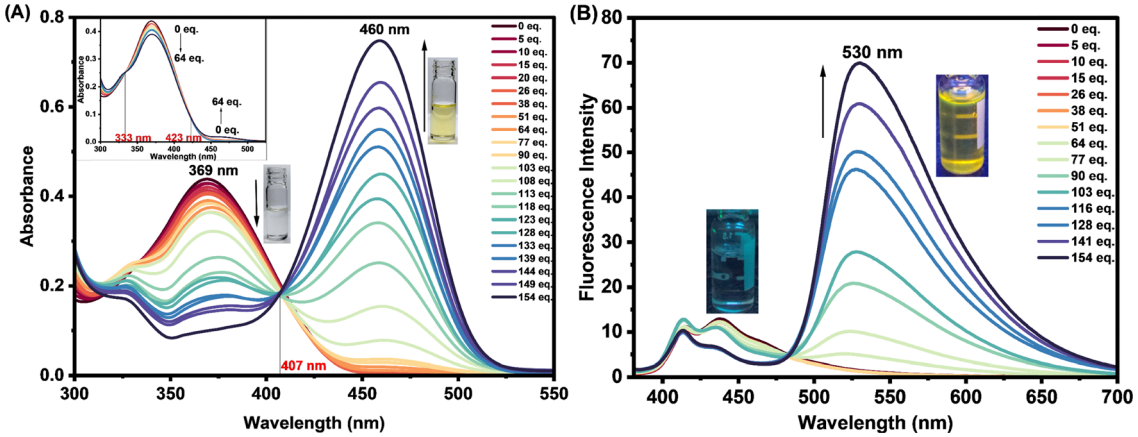

Fig. 8 (A) Absorption spectra (inset: 1st step change, images captured under white light) and (B) fluorescence spectra of compound **3** in 10^{-5} M DMSO upon the addition of sulfide ions at λ_{exc} = 369 nm (inset images are under 365 nm UV lamp).

new red-shifted absorption peak appeared at 460 nm with a distinct isobestic point at 407 nm. According to Bhattacharya's proposal, this prominent bathochromic shift of the absorption band suggests the shifting of the intramolecular charge transfer (ICT) band due to the deprotonation of the compound **3** by the sulfide anions.[47] From the colorimetric titration data, stoichiometry ratios and binding constants were determined using the Benesi–Hildebrand (B–H) method (Fig. S26). The B–H plots revealed a binding constant of 1.454×10^5 M^{-2}. The linear fitting of the B–H plot on the second power of anion concentration (R^2 = 0.99) indicated a 1 : 2 stoichiometric ratio between probe **3** and sulfide.

The fluorometric selective sensing of chemosensor compound **3** in 10^{-5} M DMSO solution upon the addition of 100 equiv. of different anions were investigated using fluorescence spectrophotometry. Interestingly, hydroxide, methoxide, and sulfide showed red-shifted emission peaks. However, due to the immense availability of hydroxide and methoxide sensors, we have focused on sulfide ions, which showed a major spectral change with a bathochromic shift from 414 nm to 530 nm (Fig. S25), along with a significant four-fold enhancement in the fluorescence emission intensity (Fig. S27). The binding properties of the chemosensor were further evaluated by systematic fluorometric titration experiments (Fig. 8B). The limit of detection (LOD) and the limit of quantitation (LOQ) were found to be 26.24 ppm and 87.48 ppm, calculated using 3σ/slope and 10σ/slope, respectively (Fig. S28). Further, the Job's plot indicated a 1 : 2 stoichiometric ratio between the chemosensor, **3**, and sulfide, which was in good agreement with the B–H plot obtained from colorimetric titration (Fig. S29). It is worth mentioning that this is the first example of an *N*-squaraine derivative to be exploited as a dual-mode colorimetric and fluorometric chemosensor for sulfide anion.

Investigation of the binding mechanism of chemosensor 3 with sulfide ions

UV-visible spectroscopic and fluorometric titration experiments demonstrated the presence of acidic –NH protons, which can form hydrogen bonding interactions in chemosensor **3**. In order to further analyze the binding mechanism of probe **3** with sulfide, ^{1}H-NMR titrations of **3** in DMSO-d_6 solvent with sulfide in D_2O were carried out to identify and study the interaction of sulfide with the acidic –NH binding sites (Fig. 9). The ^{1}H-NMR of **3** in DMSO-d_6 shows an –NH peak at 11.23 ppm. The addition of sulfide ions resulted in gradual peak broadening and upfield shift of the –NH signal from 11.23 to 10.44 ppm. Further, the successive addition of sulfide led to the complete disappearance of the –NH signal, suggesting a strong hydrogen bonding interaction between the sulfide anion and the acidic –NH protons of compound **3**. Since sulfide has strong basicity and less hydrogen bonding character with water, it tends to deprotonate the more acidic –NH protons, and the resulting negative charge is delocalized in the central squaryl acceptor core, affecting the chemical shifts of the neighbouring aromatic protons.[41,48,49] The signal at 7.54 ppm corresponding to phenyl protons split into two distinct doublets at 7.58 ppm and 7.45 ppm in the presence of sulfide ions

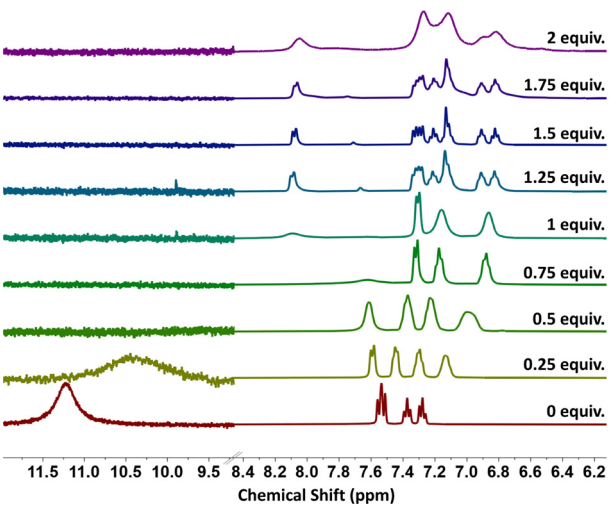

Fig. 9 ^{1}H-NMR titration of **3** in a DMSO-d_6 solvent with (0–2 equiv.) increments of sulfide in D_2O.

(0.25 equiv.), implying enhanced intramolecular charge transfer (ICT) in the system. Further addition of sulfide ions up to 1 equiv., the *o*-phenyl protons experience a downfield shift to 8.09 ppm, and an upfield shift is observed for the remaining three signals of phenyl protons till 6.86 ppm. Beyond the addition of 1 equiv. of sulfide ions, the electron distribution became unsymmetrical, resulting in major protons appearing as individual signals. However, the peak positions remained constant. This suggests that the formation of an anionic intermediate with an improved ICT after the addition of 1 equiv. of sulfide ions. Upon successive addition of sulfide ions, the electron density within the system is gradually stabilized, and finally, with the addition of 2 equiv. of sulfide ions, the symmetry within the system is regained, and ICT is strongly enhanced. Thus, the ^{1}H-NMR titrations validate the colorimetric and fluorometric sensing of sulfide ions by chemosensor **3** through the deprotonation mechanism. The plausible sensing mechanism for the interaction between chemosensor **3** and sulfide ions is illustrated in Fig. 10. Initially, one of the –NH protons is deprotonated by strongly basic sulfide, and the resultant negative charge is delocalized over the central squaryl core, forming a mono-anionic species, **3**·H$^-$. Further abstracting the other acidic –NH proton of **3**·H$^-$ by sulfide ion, forming di-anionic species, **3**$^{2-}$. Thus, the sulfide ions favor the abstraction of acidic –NH$^+$ protons *via* hydrogen bonding over the neutral protons from water molecules, thereby facilitating the detection of sulfide ions by **3**.

Reversibility of the sensor and its application in logic gate studies

The recyclability and reversibility studies of compound **3** acting as a chemosensor for sulfide ions were investigated using UV-visible absorption spectroscopy. 0.1 M acetic acid solution was used as the source of H$^+$ ions to understand the chemically reversible nature of the **3**·S^{2-} complex. Upon adding H$^+$ ions, the yellow color of **3** disappeared, and the solution turned colorless, which was the initial color of free chemosensor **3**. This discoloration implies that the binding of **3** with sulfide is chemically reversible. The subsequent addition of sulfide to this mixture resulted in the formation of the **3**·S^{2-} complex again, which was detected from the reappearance of yellow color. The UV-visible absorbance studies supported the above findings, and the absorption intensity at 460 nm plunged upon the addition of H$^+$ ions, and the addition of sulfide ions revived back the intensity at 460 nm. The chemosensor **3** was sustainable for seven cycles of alternate additions of sulfide and H$^+$ ions with trivial spectral deviations, as shown in Fig. 11, thereby exhibiting significant reversibility without losing substantial sensitivity up to seven cycles. The reversibility mechanism of sensing sulfide ions and retrieving free compound **3** with H$^+$ ions involves rapid deprotonation and then protonation steps, respectively. Firstly, the chemosensor **3** forms a hydrogen bonding interaction with sulfide ions through the two NH binding sites, causing deprotonation. The ICT mechanism facilitates this interaction, causing a color change from colorless to yellow with a bathochromic shift in its absorption spectra. Then, adding H$^+$ ions breaks the initial hydrogen-bonded interaction formed between sulfide and the –NH binding sites of chemosensor **3**, by forming a stronger ionic interaction between sulfide and H$^+$ ions and protonating chemosensor **3** back to its original form.

A two-input molecular logic gate was developed by taking into account the reversibility and reproducible nature of chemosensor **3** upon alternate additions of sulfide and H$^+$ ions (Fig. 12). A combination of additions of sulfide and H$^+$ was analyzed, and the corresponding variations in the spectra were denoted as the output. Two outputs were fixed based on the absorption intensity from two inputs for chemosensor **3**. For the output, high absorption or intensity peaks were designated as ''1'', and low-intensity or absent peaks were designated as

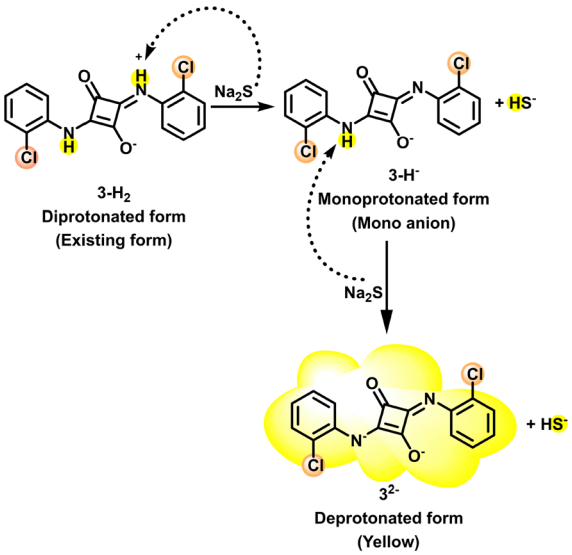

Fig. 10 Plausible sensing mechanism between **3** and sulfide.

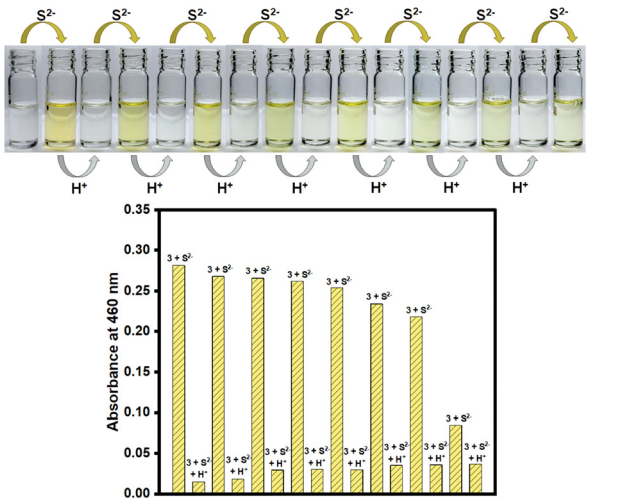

Fig. 11 Reversibility of chemosensor **3** with alternate additions of S^{2-} and H$^+$ (CH_3COOH) ions, monitoring the changes in absorption at 460 nm for eight cycles.

TRUTH TABLE			
INPUT		OUTPUT	
1 S^{2-}	2 H^+	1 Abs at 369 nm	2 Abs at 460 nm
0	0	1	0
1	0	0	1
0	1	1	0
1	1	1	0

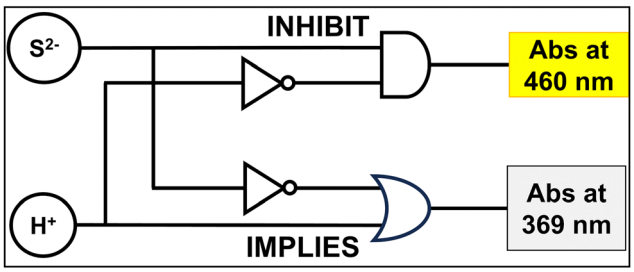

Fig. 12 The complementary "INHIBIT" and "IMPLIES" logic gate with the truth table for chemosensor **3** shows a yellow color change in the presence of S^{2-} and the absence of H^+ ions.

"0". The absorption intensity at 460 nm is high only in the presence of sulfide ions and in the absence or at a lower concentration of H^+ ions. Other combinations failed to enhance the absorption intensity at 460 nm, and therefore, this is an example of an "INHIBIT" logic gate (Fig. 12). Likewise, the absorption intensity at 369 nm corresponds to free chemosensor **3**, which is retained in all the combinations, except for the presence of sulfide with low or no H^+, which is an example of the "IMPLIES" logic gate (Fig. 12).

Conclusions

In conclusion, symmetric *N*-squaraines having fluoro, chloro, bromo, and iodo functional groups at the *ortho* positions of phenyl rings were synthesized. The spectroscopic characterization and single-crystal X-ray diffraction studies validated the structure of the molecules. The incorporation of halogens at *ortho* positions significantly tailored the photophysical and electrochemical properties, giving rise to a hypsochromic shift in absorption compared to compound **1**. The compounds **1–5** in DMSO exhibited negligible fluorescence with their quantum yields below unity. However, the addition of NaOH resulted in a bathochromic shift of ~90 nm in absorption spectra due to extended π-conjugation and enhanced emission intensity with improved quantum yields as a result of ICT. Moreover, the compounds exhibit solid-state emissive behavior, with compound **2** showing the highest quantum yield of 24%. Furthermore, the colorimetric and fluorometric anion-binding studies revealed that compound **3** effectively binds sulfide with a 1 : 2 stoichiometry. The chemosensor **3** revealed remarkable recyclability for up to seven cycles without losing sensitivity. The chemosensor **3** was utilized in molecular logic gates. We believe this study indeed opens new avenues for the development of *N*-squaraines with a wide range of applications in the field of material science.

Conflicts of interest

There are no conflicts to declare.

Data availability

The data supporting this article have been included as part of the supplementary information (SI). Supplementary information: ^{1}H-NMR; HRMS; FT-IR; X-ray diffraction structure and crystal data of compound **2** (CCDC no. 2388391); DFT coordinates; UV-visible absorption and fluorescence spectra; TCSPC decay plots; sensing studies. see DOI: **https://doi.org/10.1039/d5tc02572a**.

CCDC 2388391 contains the supplementary crystallographic data for this paper.[50]

Acknowledgements

V. L. acknowledges the Science and Engineering Research Board (SERB), India, for partially supporting through the SRG (2021/002251) grant. P. P. F., A. M. S., and V. G. thank NITK for the institute research fellowship, UGC for the SJSGC fellowship, and CSIR, India, for a fellowship, respectively. The authors gratefully acknowledge the Department of Chemistry, NITK, CRF-NITK, SCIF-IIT Dharwad, and the Department of Chemistry, IIT Bombay.

References

1 M. Vega, R. M. Gomila, J. Pons, A. Frontera, C. Rotger and A. Costa, *Dyes Pigm.*, 2022, **207**, 110746.
2 J. He, Y. J. Jo, X. Sun, W. Qiao, J. Ok, T. Kim and Z. Li, *Adv. Funct. Mater.*, 2021, **31**, 2008201.
3 Q. Xiao, S. Yang, R. Wang, Y. Zhang, H. Zhang, H. Zhou and Z. Li, *Dyes Pigm.*, 2018, **154**, 137–144.
4 K. Y. Law, *Chem. Rev.*, 1993, **93**, 449–486.
5 M. Gsänger, D. Bialas, L. Huang, M. Stolte and F. Würthner, *Adv. Mater.*, 2016, **28**, 3615–3645.
6 S. Sreejith, P. Carol, P. Chithra and A. Ajayaghosh, *J. Mater. Chem.*, 2008, **18**, 264–274.
7 J. V. Ros-Lis, R. Martínez-Máñez, F. Sancenón, J. Soto, M. Spieles and K. Rurack, *Chem. – Eur. J.*, 2008, **14**, 10101–10114.
8 I. A. Karpenko, M. Collot, L. Richert, C. Valencia, P. Villa, Y. Mély, M. Hibert, D. Bonnet and A. S. Klymchenko, *J. Am. Chem. Soc.*, 2015, **137**, 405–412.
9 M. Vega, S. Blasco, E. GarcíaEspaña, B. Soberats, A. Frontera, C. Rotger and A. Costa, *Dalton Trans.*, 2021, **50**, 9367–9371.
10 G. Xia, Y. Liu, B. Ye, J. Sun and H. Wang, *Chem. Commun.*, 2015, **51**, 13802–13805.
11 W. Yang, G. Yang, X. Jia, L. Wu and R. Wang, *J. Physiol.*, 2005, **569**, 519–531.

12 M. M. Gadalla and S. H. Snyder, *J. Neurochem.*, 2010, **113**, 14–26.
13 F. Yuan, X. He, Y. Lu, L. Ning, X. Zhao, S. Zhang, F. Guan, Y. Guo and J. Zhang, *Anal. Chem.*, 2023, **95**, 6931–6939.
14 F. Zhang, A. Zhu, Y. Luo, Y. Tian, J. Yang and Y. Qin, *J. Phys. Chem. C*, 2010, **114**, 19214–19219.
15 B. D. Paul, J. I. Sbodio, R. Xu, M. S. Vandiver, J. Y. Cha, A. M. Snowman and S. H. Snyder, *Nature*, 2014, **509**, 96–100.
16 R. M. Mandel, P. S. Lotlikar, T. Runčevski, J. H. Lee, J. J. Woods, T. A. Pitt, J. J. Wilson and P. J. Milner, *J. Am. Chem. Soc.*, 2024, **146**, 18927–18937.
17 P. Kamoun, M. Belardinelli, A. Chabli, K. Lallouchi and B. Chadefaux-Vekemans, *Am. J. Med. Genet., Part A*, 2003, **116A**, 310–311.
18 S. Fiorucci, E. Antonelli, A. Mencarelli, S. Orlandi, B. Renga, G. Rizzo, E. Distrutti, V. Shah and A. Morelli, *Hepatology*, 2005, **42**, 539–548.
19 R. O. Beauchamp, J. S. Bus, J. A. Popp, C. J. Boreiko, D. A. Andjelkovich and P. Leber, *Crit. Rev. Toxicol.*, 1984, **13**, 25–97.
20 R. J. Reiffenstein, W. C. Hulbert and S. H. Roth, *Annu. Rev. Pharmacol. Toxicol.*, 1992, **32**, 109–134.
21 Z. Zhang, Z. Chen, S. Wang, C. Qu and L. Chen, *ACS Appl. Mater. Interfaces*, 2014, **6**, 6300–6307.
22 S. Y. Lee and C. Kim, *RSC Adv.*, 2016, **6**, 85091–85099.
23 N. S. Lawrence, L. Jiang, T. G. J. Jones and R. G. Compton, *Anal. Chem.*, 2003, **75**, 2054–2059.
24 M. Deb, C. J. Lu and H. W. Zan, *ACS Sens.*, 2024, **9**, 4568–4577.
25 M. Colon, J. L. Todolí, M. Hidalgo and M. Iglesias, *Anal. Chim. Acta*, 2008, **609**, 160–168.
26 C. Song, J. J. Lee, H. Nam and C. Kim, *Korean J. Chem. Eng.*, 2025, **42**, 669–678.
27 K. Sasakura, K. Hanaoka, N. Shibuya, Y. Mikami, Y. Kimura, T. Komatsu, T. Ueno, T. Terai, H. Kimura and T. Nagano, *J. Am. Chem. Soc.*, 2011, **133**, 18003–18005.
28 F. J. Huo, J. Kang, C. Yin, J. Chao and Y. Zhang, *Sci. Rep.*, 2015, **5**, 8969.
29 Y. Chen, J. Bao, Q. Wang, M. S. Hameed, S. Tang, Q. Chen, H. Fan, J. Yan, G. Yang, K. Zhang and X. Han, *Anal. Chem.*, 2025, **97**, 721–730.
30 Y. Yan, L. Chen, R. Liu, Y. Zheng and S. Wang, *RSC Adv.*, 2019, **9**, 27652–27658.
31 X. Wei, L. Mi, S. Dong, H. Yang and S. Xu, *RSC Adv.*, 2024, **14**, 16327–16331.
32 Z. Liang, T. H. Tsoi, C. F. Chan, L. Dai, Y. Wu, G. Du, L. Zhu, C. S. Lee, W. T. Wong, G. L. Law and K. L. Wong, *Chem. Sci.*, 2016, **7**, 2151–2156.
33 X. Li, J. Cheng, Y. Gong, B. Yang and Y. Hu, *Biosens. Bioelectron.*, 2015, **65**, 302–306.
34 S. Y. Lee and C. Kim, *RSC Adv.*, 2016, **6**, 85091–85099.
35 F. J. Huo, J. Kang, C. Yin, J. Chao and Y. Zhang, *Sci. Rep.*, 2015, **5**, 8969.
36 M. M. Fortibui, D. W. Yoon, J. Y. Lim, S. Lee, M. Choi, J. S. Heo, J. Kim and J. Kim, *Dalton Trans.*, 2021, **50**, 2545–2554.
37 J. Cheng, J. Song, H. Niu, J. Tang, D. Zhang, Y. Zhao and Y. Ye, *New J. Chem.*, 2016, **40**, 6384–6388.
38 N. Adarsh, M. S. Krishnan and D. Ramaiah, *Anal. Chem.*, 2014, **86**, 9335–9342.
39 S. Gupta, G. Kumar, V. Luxami and K. Paul, *Mater. Adv.*, 2025, **6**, 4389–4401.
40 K. G. Fosnacht and M. D. Pluth, *Chem. Rev.*, 2024, **124**, 4124–4257.
41 M. Ranjana, R. M. Kulkarni and D. Sunil, *ACS Omega*, 2024, **9**, 14672–14691.
42 S. Enoch, A. B. Nipate, V. Lakshmi and R. R. Malakalapalli, *Chem. Commun.*, 2023, **59**, 8846–8849.
43 N. S. Veeranagaiah, B. Borah, S. N. Dhuri, R. Pallepogu and L. R. Chowhan, *J. Mol. Struct.*, 2025, **1321**, 140229.
44 W. Hu, R. Zhang, X. F. Zhang, J. Liu and L. Luo, *Spectrochim. Acta, Part A*, 2022, **272**, 120965.
45 K. Yamamoto, A. Takagi, M. Hada, R. Taniwaki, T. Mizutani, Y. Kimura, Y. Takao, K. Moriwaki, F. Matsumoto, T. Ito, T. Iwai, K. Hida, T. Mizuno and T. Ohno, *Tetrahedron*, 2016, **72**, 4918–4924.
46 S. Y. Park, K. Jun and S. W. Oh, *Bull. Korean Chem. Soc.*, 2005, **26**, 428–432.
47 N. Kumari, S. Jha and S. Bhattacharya, *J. Org. Chem.*, 2011, **76**, 8215–8222.
48 J. H. Kang, J. B. Chae and C. Kim, *R. Soc. Open Sci.*, 2018, **5**, 180293.
49 A. K. Manna, J. Mondal, R. Chandra, K. Rout and G. K. Patra, *Anal. Methods*, 2018, **10**, 2317–2326.
50 CCDC 2388391: Experimental Crystal Structure Determination, 2025, DOI: **10.5517/ccdc.csd.cc2l59wz**.

